Journal of Materials Chemistry B

ROYAL SOCIETY OF CHEMISTRY

PAPER

View Article Online
View Journal | View Issue

Cite this: J. Mater. Chem. B, 2025, 13, 15389

Focused ultrasound propulsion of acoustically active nanoparticles into gelatin hydrogels

Talaial B. Alina,[a] Shane D. Curry,[a] Sven A. Saemundsson,[a] Bryce M. Bower,[a] Jennifer N. Cha *[abc] and Andrew P. Goodwin *[ab]

Dense biological tissues present formidable transport barriers that limit therapeutic penetration. Ultrasound-mediated propulsion can help to cross these barriers, but the presence of viscoelastic media can dampen ultrasonic cavitation and particle movement. The effect of gelatin (2–8% w/v) hydrogel mechanical properties (G' ~100–2100 Pa) on cavitation-mediated nanoparticle transport was tested using phospholipid-coated, hydrophobically modified mesoporous silica nanoparticles (DBPC HMSNs) and high-intensity focused ultrasound (HIFU). The minimum duty cycle required for effective penetration increased with hydrogel stiffness: 0.5% for 2% gelatin, 1.0% for 4% gelatin, and 3.6% for 8% gelatin. Soft hydrogels (2–4%) developed localized microchannels and release of gelatin from the gels only when treated with DBPC HMSNs under HIFU, but maintained their bulk mechanical properties. Stiff 8% gelatin exhibited organized honeycomb structures with 20–40% modulus reduction and amine release even in non-cavitating controls, indicating bulk weakening across all treatment groups. Non-cavitating control particles (unmodified MSNs) showed minimal penetration across all conditions, confirming cavitation as the primary driver of particle transport. SEM revealed treatment-dependent morphological changes across all HIFU-treated gels, including the formation of micropores and organized structures. These findings reveal that soft hydrogels (100–450 Pa) allow localized cavitation-mediated transport while preserving bulk integrity, whereas stiffer (>1000 Pa) hydrogels require higher acoustic intensities that inevitably cause bulk mechanical weakening. This stiffness-dependent response suggests that effective translation to biological barriers will require matching ultrasound parameters to target tissue mechanics.

Received 24th July 2025,
Accepted 23rd October 2025

DOI: 10.1039/d5tb01702e

rsc.li/materials-b

1. Introduction

Ultrasound can enhance drug delivery by increasing molecular and/or particulate motion, as well as tissue permeability, through mechanical effects. However, the intensities required to achieve these effects depend on tissue density and barrier properties. Diagnostic ultrasound (I_{SPTA}: < 0.3 W cm^{-2}), widely used for non-invasive imaging, produces insufficient energy density to achieve these goals.[1] Low-intensity focused ultrasound (LIFU; I_{SPTA}: 0.03–0.50 W cm^{-2})[2] can produce mechanical effects such as neuromodulation that temporarily increase the permeability of cell membranes and tissue barriers. Applications include transdermal drug delivery.[3]

For denser tissues with significant transport barriers, high-intensity focused ultrasound (HIFU) is required,[4] in which ultrasonic pulses are focused into millimeter-scale focal regions. HIFU achieves intensities (I_{SPTA}) of 10^2–10^4 W cm^{-2}, usually to achieve therapeutic effects.[5] Clinical uses of HIFU include uterine fibroid ablation[6] and focal prostate cancer therapy.[7]

Operating at low duty cycles (≤5%) can limit bulk temperature rise while emphasizing mechanical effects such as stable cavitation, microstreaming, and inertial cavitation.[8–10] This rapid microbubble expansion and violent bubble collapse from inertial cavitation can generate localized stresses capable of killing cells, fracturing polymer networks, and creating transient transport pathways.[11,12] These effects may be desired at specific locations but are prone to damaging off-target, healthy tissue. Furthermore, degradation of the tumor stroma can inadvertently promote cancer cell invasion and metastasis.[13,14]

To enhance cavitation at sub-therapeutic intensities and pressures, our group constructed 100 nm phospholipid-capped, hydrophobically modified mesoporous silica nanoparticles (PL-HMSNs) as cavitation nuclei. These nanoparticles reduce the cavitation threshold to as low as ~7 MPa negative pressure and remain active at concentrations as low as 12.5 μg mL^{-1}.[15,16] HIFU with PL-HMSNs allows usage of sub-therapeutic ultrasound intensities to limit off-target effects. Unlike μm-scale microbubbles confined to the vasculature, nanoscale PL-HMSNs can potentially extravasate

[a] Department of Chemical and Biological Engineering, USA
[b] Materials Science and Engineering Program, USA
[c] Biomedical Engineering Program, University of Colorado Boulder, Boulder, Colorado, 80303, USA. E-mail: jennifer.cha@colorado.edu, andrew.goodwin@colorado.edu

into interstitial spaces and enable systemic delivery followed by targeted activation at the ultrasound focus.[17,18] This approach has potential applications in blood–brain barrier opening, immunomodulation, and improved intratumoral drug distribution.[19,20] Finally, the induction of cavitation on the particle surface was recently shown to promote its propulsion through fluids, with speeds in water reaching 1600 μm s^{-1} and displacements of 250 μm through cavitation-mediated mechanisms.[21]

In practice, however, many areas of interest for this ultrasound-mediated drug delivery approach have viscoelastic properties. Material stiffness influences local acoustic behavior, with studies showing reductions in maximum ultrasound intensity and increases in attenuation coefficients as viscoelasticity increases in both gelatin[21] and polyacrylamide[22] hydrogels. For example, passive cavitation detection studies in ultrapure water/PEG 2000 mixtures demonstrate that increased viscosity elevates cavitation thresholds (Fig. S1).[23] Building on these findings, this study employs gelatin hydrogels as tissue-mimicking phantoms with tunable mechanical properties.[24] Gelatin, derived from denatured collagen, forms physically crosslinked networks whose viscoelastic properties can be precisely controlled *via* polymer concentration, displaying storage (G') and loss moduli (G'') that mimic the elastic and viscous behavior of target tissues.[25,26] Gelatin hydrogels can achieve elastic moduli >100 kPa depending on concentration[21] and crosslinking.[27] However, the present study focuses on the lower range (up to 2 kPa) relevant for modelling highly compliant tissues such as bone marrow (0.25 to 24.7 kPa),[28] a healthy human liver (0.5 to 1 kPa),[29] brain tissue (1–2 kPa),[30] and lung tissue (1–5 kPa).[31]

This work tests the hypotheses that (i) increasing gelatin concentration and hydrogel storage modulus will elevate the duty cycle threshold required for cavitation-mediated transport, and (ii) because cavitation is only expected to occur at the ultrasound focus, the bulk properties of the gelatin will remain mostly unchanged. Rheometry and fluorescence imaging are employed to assess mechanical changes and nanoparticle penetration following HIFU exposure. This approach identifies optimal acoustic parameters that enhance transport without compromising surrounding gel integrity. Unmodified mesoporous silica nanoparticles (MSNs) serve as controls to isolate the specific effects of the phospholipid coating on cavitation-enhanced transport. These fundamental relationships obtained in this model system will provide design principles for optimizing HIFU conditions to target biological barriers to drug delivery.

2. Experimental

Note: detailed experimental procedures, including names of chemical and equipment suppliers, can be found in Supplementary Information.

2.1. Nanoparticle synthesis and functionalization

Mesoporous silica nanoparticles (MSNs) were synthesized using a cetyltrimethylammonium chloride (CTAC)-templated sol–gel method and fluorescently labelled with *N*-hydroxysuccinimide rhodamine (NHS-rhodamine). Hydrophobic surface modification was achieved *via* reaction with octadecyltrichlorosilane (ODTS) in anhydrous dichloromethane to yield hydrophobically modified MSNs (HMSNs). Lipid coating of HMSNs was performed *via* solvent exchange using 1,2-dibehenoyl-*sn-glycero*-3-phosphocholine (DBPC) and 1,2-distearoyl-*sn-glycero*-3-phosphoethanolamine-*N*-[methoxy-(polyethylene glycol)-2000] (DSPE-PEG2K-methoxy), resulting in phospholipid-coated HMSNs (PL-HMSNs).

2.2. Nanoparticle characterization

Nanoparticles were characterized by dynamic light scattering (DLS) and zeta potential measurements in 1X PBS. Surface chemical modifications were confirmed using diffuse reflectance infrared Fourier transform spectroscopy (DRIFTS).

2.3. Hydrogel preparation

Gelatin hydrogels (2%, 4%, and 8% w/v) were prepared by diluting a mixture of 17% (w/v) gelatin and 1% (w/v) sodium azide with 1X PBS to achieve the desired final concentrations. Gels were cast as cylindrical molds formed in plastic transfer pipettes and allowed to set overnight at room temperature.

2.4. Ultrasound insonation and cavitation characterization

High-intensity focused ultrasound (HIFU) was applied using a 1.1 MHz transducer coupled to a waveform generator and power amplifier. Cavitation behavior was characterized using passive cavitation detection (PCD) with a 20 MHz transducer and high-pass filtering. Duty cycles ranged from 0 to 3.6%, corresponding to 0–40 cycles per pulse.

2.5. Transport assay in gelatin gels

PL-HMSNs and MSNs (200 μg mL^{-1}) were introduced into a pipette-bulb chamber sealed to the hydrogel interface. High-intensity focused ultrasound (HIFU) insonation was applied for 1 min. Following treatment, hydrogels were carefully sliced both transversely and longitudinally to expose internal regions. Nanoparticle transport into the gel was then visualized by confocal fluorescence microscopy using 561 nm excitation and tile-stitching.

2.6. Post-treatment analysis

Rheological properties of treated gels were measured by parallel plate rheometry. Amine release from the hydrogel matrix was quantified by trinitrobenzenesulfonic acid (TNBS) assay. Structural changes in the hydrogel network were visualized by SEM, with pore morphology analyzed using Python-based image processing pipelines.[32]

2.7. Image and data analysis

Custom Python workflows were used for semi-automated image analysis of gel geometry, interface morphology, and nanoparticle penetration. These tools included modules for ROI selection, baseline correction, curved interface analysis, and overlay-based quantification of particle distribution and penetration area.[32]

3. Results and discussion

3.1. Synthesis and surface functionalization of DBPC-HMSNs

Following previously established protocols,[16,33] fluorescently-tagged mesoporous silica nanoparticles (MSNs) were synthesized, hydrophobically modified with octadecyltrichlorosilane (ODTS) to form HMSNs, and subsequently coated with a lipid bilayer of 1,2-dibehenoyl-*sn-glycero*-3-phosphocholine (DBPC) and 1,2-distearoyl-*sn-glycero*-3-phosphoethanolamine-(polyethylene glycol)-2000 (DSPE-PEG2K-methoxy) to yield the final DBPC HMSN particles for aqueous stabilization (Fig. 1A). The particle surface chemistry was assessed in each synthetic step using diffuse reflectance infrared Fourier-transformed infrared spectroscopy (DRIFTS) (Fig. 1B). The spectrum for the precursor MSNs showed a characteristic peak for Si–O stretching vibrations of Si–O–H at approximately 960 cm^{-1}.[33,34] After modification, the resulting HMSNs exhibited new peaks corresponding to C–H stretching in the 3000–2800 cm^{-1} region, specifically at 2926 cm^{-1} and 2854 cm^{-1}. This confirms the successful functionalization with the octadecyl alkyl chains necessary to promote acoustic cavitation.[33,35]

3.2. Colloidal stability in 1X PBS

Next, the particles physical and colloidal properties in aqueous solution were determined by dynamic light scattering (DLS) and zeta potential measurements in 1X phosphate-buffered saline (PBS, Fig. 1C and D). Number-weighted DLS in 1X PBS revealed that uncoated MSNs displayed a single population at 97.2 ± 19.2 nm (Fig. 1C). Following hydrophobic modification and lipid addition, DBPC HMSNs exhibited a dominant peak at 229.8 ± 26.9 nm and a minor aggregate population at 2155.5 ± 419.5 nm. Zeta potential measurements support these results: MSNs had a surface charge of −15.0 ± 0.5 mV, while DBPC HMSNs approached neutrality at −1.0 ± 0.4 mV (Fig. 1D).

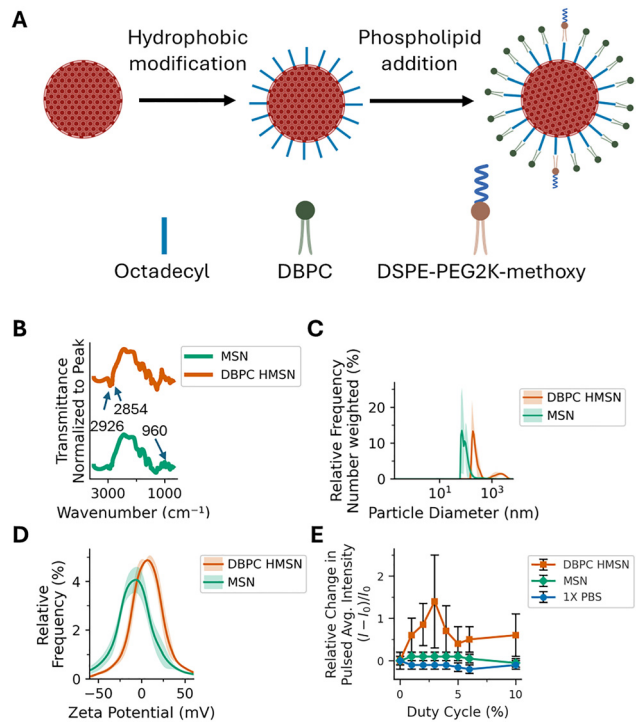

Fig. 1 (A) Schematic of DBPC HMSN synthesis. (B–D) MSN and DBPC HMSN: (B) diffuse reflectance infrared Fourier transform spectroscopy (DRIFTS, n = 1), (C) dynamic light scattering (DLS, n = 3) in 1X PBS, (D) zeta potential (n = 3) in 1X PBS, (E) passive cavitation detection studies (n = 3) including 1X PBS. Error bars (B) and shading (C) and (D) signify one standard deviation of the mean.

3.3. Cavitation activity under HIFU

The cavitation response of the successfully modified particles was measured using passive cavitation detection (PCD) by applying high-intensity focused ultrasound (HIFU) at varying duty cycles. The control samples without particles (1X PBS) or with unmodified MSNs produced minimal acoustic signal near the baseline noise level (Fig. 1E). In contrast, DBPC HMSNs generated a robust cavitation signal that increased with the duty cycle. For DBPC HMSNs, an apparent decrease in received cavitation signal is observed above 2.5% duty cycle; however, in previous studies a decrease in signal at higher intensities has been observed, which is attributed to formed bubbles attenuating the emitted signal.[33] It was also determined separately that DBPC HMSNs could promote cavitation in 1, 5, and 20 cP PEG2000 aqueous solutions (Fig. S1). These findings demonstrate that the hydrophobic surface of the DBPC HMSNs effectively facilitates inertial cavitation, as consistent with previous work by the authors.[16,33,36]

3.4. Particle transport into gelatin hydrogels

With the acoustic activity of the DBPC HMSNs confirmed and the MSNs established as negative controls, two hypotheses were tested: (i) if the minimum duty cycle required for effective nanoparticle penetration would increase with hydrogel stiffness, and (ii) if cavitation-mediated transport will create localized microchannels without measurably altering the gel's bulk viscoelastic properties. To investigate this, a gelatin hydrogel was fabricated inside an inverted transfer pipette (Fig. 2A). Next, HIFU was applied to a solution of particles in the transfer pipette bulb to facilitate cavitation and drive particle penetration into the hydrogel. After HIFU treatment, gels were removed from the pipette molds by making a longitudinal razor cut on a flat support board, then transversely sectioned into ~2 mm slices and placed on glass slides. Immediately before imaging, each slice was immersed in a sucrose solution (2.5–10% w/v, depending on gelatin concentration) to match its refractive index and minimize light scattering (Fig. 2B).

The penetration areas of fluorescent particles in 2%, 4%, and 8% gelatin hydrogels were quantified following ultrasound exposure (Fig. 3A). DBPC HMSNs demonstrated cavitation onset at ≥0.5% duty cycle across all gel concentrations. However, substantial particle penetration required higher duty cycles that increased with gel stiffness: 0.5% for 2% gelatin, 1.0% for 4% gelatin, and 3.6% for 8% gelatin. In contrast, non-cavitating MSNs showed minimal penetration at all duty cycles tested. Higher duty cycles induced bulk thermal melting: a 3.6% duty cycle melted 2% and 4% gelatin, while a 5.0% duty cycle melted

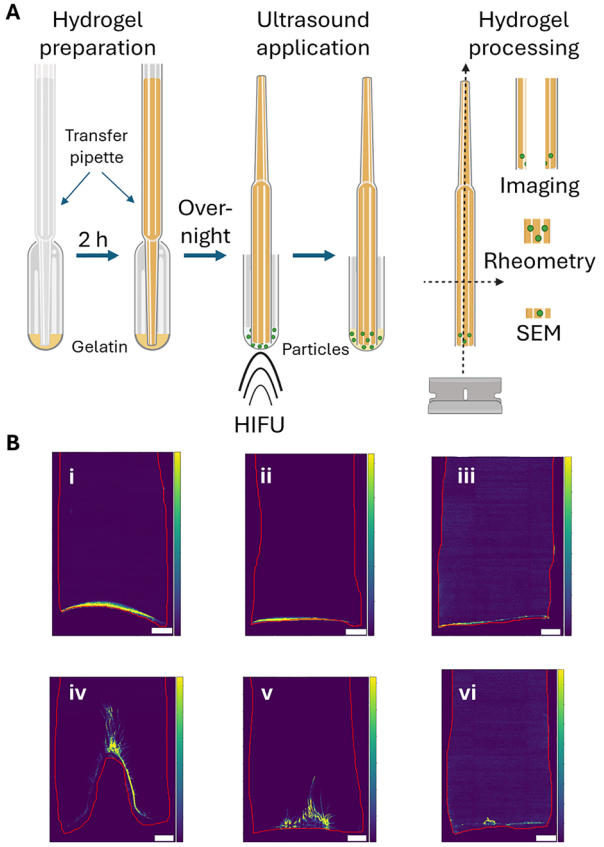

Fig. 2 (A) Schematic of gel preparation, HIFU treatment, and preparation for characterization. (B) Confocal microscopy images of particle penetration into gelatin hydrogels after HIFU. Pseudocolor scale indicates fluorescence intensity, ranging from low (bottom of colorbar) to high (top). Scale bar = 1 mm. Top row (i)–(iii): hydrogels treated with MSNs; bottom row (iv)–(vi): hydrogels treated with DBPC HMSNs. Columns (left to right): 2% and 4% gelatin imaged after a 2.5% duty-cycle treatment, and 8% gelatin imaged after a 3.6% duty-cycle treatment.

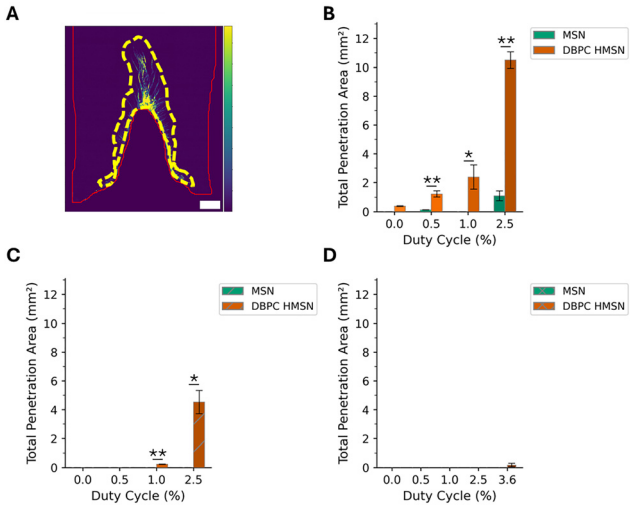

Fig. 3 (A) Representative dashed outline (yellow) of the penetration area in 2% gelatin. Pseudocolor scale indicates fluorescence intensity, ranging from low (bottom of colorbar) to high (top). Scale bar = 1 mm. Penetration area (n = 3) of MSNs and DBPC HMSNs driven into (B) 2%, (C) 4%, and (D) 8% gelatin. Error bars signify one standard deviation of mean. Statistical significance between the no HIFU and HIFU groups was tested using a one-tailed independent-samples Welch's t-test (*$p < 0.05$, **$p < 0.01$).

8% gelatin. Therefore, tested duty cycles were kept below conditions of gelatin melting.

At 2.5% duty cycle, DBPC HMSNs achieved significantly greater penetration than MSNs in both 2% (Fig. 3B, *$p < 0.05$, **$p < 0.01$) and 4% gelatin (Fig. 3C, *$p < 0.05$, **$p < 0.01$). While MSNs showed a modest signal increase at 2.5% duty cycle, this likely resulted from localized heating rather than cavitation-mediated transport, as no cavitation was detected for MSNs under identical conditions. This interpretation is supported by temperature measurements, which showed only a temperature rise of 4–7 °C near the focal zone across all samples during treatment (Fig. S2). This heating effect is insufficient to explain the large penetration areas achieved with DBPC HMSNs only, confirming that inertial cavitation is the dominant transport mechanism. In 8% gelatin at 3.6% duty cycle, DBPC HMSNs achieved higher penetration than MSNs (0.20 mm^2 *vs.* 0 mm^2), though the difference was not statistically significant (Fig. 3D).

Additionally, the influence of nanoparticle concentration on transport was investigated. HIFU treatment of a lower particle concentration of 25 μg mL^{-1} produced a greater penetration area than the higher 200 μg mL^{-1} concentration for both particle types, though this difference was not statistically significant (Fig. S3). This observation is consistent with previous reports in which higher particle concentrations may attenuate ultrasound, thereby limiting the energy delivered to the focal region and reducing dampening cavitation-driven transport.[37]

Together, these results demonstrate that DBPC HMSNs harness inertial cavitation to overcome the elastic and viscous resistance of softer hydrogels (2–4% gelatin), whereas increasing network stiffness in 8% gelatin markedly limits cavitation-mediated transport. The influence of gelatin concentration on nanoparticle transport into the hydrogel can be attributed to two related factors. First, increased material stiffness and viscoelasticity provide greater mechanical resistance to bubble expansion and collapse.[11] Higher hydrogel modulus also shrinks the network's mesh size and directly impedes nanoparticle mobility[38] by imposing additional drag.[39] Second, denser gelatin phantoms exhibit stronger ultrasound attenuation, reducing the acoustic intensity delivered to the focal zone.[21] The combined effect produces smaller, more spatially confined cavitation zones in stiffer gels, explaining the reduced penetration areas observed at 8% as compared to 4% and 2% gelatin. From a translational perspective, these findings suggest that fibrotic or collagen-dense tissues may require higher acoustic power or more potent nucleating agents to achieve therapeutic outcomes comparable to those in softer tissues.

3.5. Mechanical response of hydrogels to cavitation

The successful transport of DBPC HMSNs prompted the question: what mechanical or structural changes occur in the gelatin hydrogel during particle propulsion? To investigate this,

parallel plate rheology was used to measure the storage modulus (G') before and after treatment (Fig. 4). Treated gel samples were prepared by cutting 4 mm-high segments from the bottom of the transfer pipette for testing. In 2% gelatin, G' remained at ~100 Pa before and after HIFU (Fig. 4A), and in 4% gelatin, it stayed at about 450 Pa (Fig. 4B), with no significant differences across any particle or control groups. These results indicated that localized cavitation events did not measurably alter the bulk elastic network.

By contrast, in 8% gelatin at 3.6% duty cycle (Fig. 4C), DBPC HMSN treated hydrogels showed a ~40% reduction in G' (from ~2100 Pa to ~1250 Pa, $*p < 0.05$), while MSN treated hydrogels decreased by ~20% (from ~2100 Pa to ~1700 Pa, $**p < 0.01$) and 1X PBS by ~25% (from ~1950 Pa to ~1500 Pa, $**p < 0.01$). 8% gelatin was insonated at a higher duty cycle than 2% and 4% gelatin gels because particle penetration was only observed at 3.6% duty cycle. Because only the stiffest matrix exhibited modulus loss, and only DBPC HMSNs penetrated the 8% gel, it is inferred that penetration in these higher-stiffness hydrogels required actual damage to the bulk network. This finding aligns with previous work showing that stiffer gels required higher mechanical inputs for cavitation.[40] While softer gels (2% and 4%) accommodate bubble expansion through elastic deformation, the high modulus of 8% gelatin (~2100 Pa) constrains bubble dynamics. Notably, all treatment groups in 8% gelatin showed storage modulus reduction at this high duty cycle, suggesting broader HIFU-induced mechanical weakening to the gelatin network.

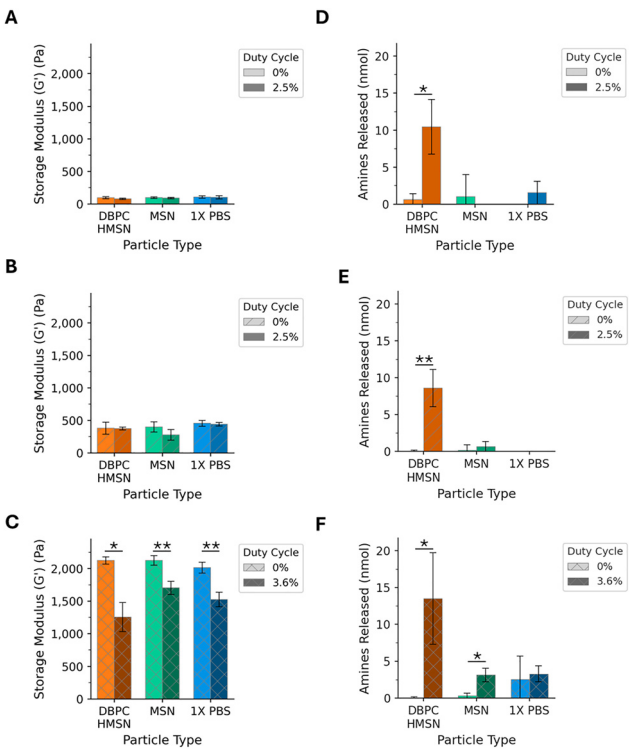

Fig. 4 Storage modulus (G') of (A) 2% gelatin, (B) 4% gelatin, and (C) 8% gelatin treated with MSNs, DBPC HMSNs, and 1X PBS (no particles) (n = 3). Error bars signify one standard deviation of mean. Statistical significance between the no HIFU and HIFU groups was tested using a one-tailed independent-samples Welch's t-test ($*p < 0.05$, $**p < 0.01$). (D)–(F) Trinitrobenzenesulfonic (TNBS) acid assays (n = 3) of (D) 2% gelatin, (E) 4% gelatin, and (F) 8% gelatin treated with MSNs, DBPC HMSNs, and 1X PBS. Error bars signify one standard deviation of mean. Statistical significance between the no HIFU and HIFU groups was tested using a one-tailed independent-samples Welch's t-test ($*p < 0.05$, $**p < 0.01$).

3.6. Location-dependence of nanoparticle transport and gel damage

Spatially-resolved analysis was next performed to probe for localized damage not apparent in the bulk measurements. Analysis of the penetration profiles revealed two key features. First, particle transport was localized, peaking in penetration area near the HIFU source (Fig. S4 and S5). Second, these profiles became narrower and shallower as gel stiffness increased. This localized transport pattern corresponded to localized mechanical damage in gels treated with cavitating nanoparticles (Fig. S6 and S8). The bottom (0–4 mm) layer of 2% and 8% gelatin treated with DBPC HMSNs softened significantly compared to the top (4–8 mm) layer ($*p < 0.05$). 4% gels showed the same directional decrease but did not reach significance. Overall, cavitating nanoparticles create local damage at the focus rather than regions farther into the gel, with the strongest local damage seen in the stiffest 8% gels.

3.7. Cavitation-induced molecular damage in hydrogels

These results prompted an investigation into whether these changes corresponded to molecular-level damage in the polymer network,[41] which was tested using the trinitrobenzenesulfonic (TNBS) acid assay. This assay quantifies primary amines released from the gelatin structure into the feed solution during HIFU treatment, though it cannot distinguish between intact and fragmented gelatin. At each gelatin concentration, DBPC HMSN treated hydrogels released significantly more primary amines under HIFU than the no-HIFU controls did ($*p < 0.05$, $**p < 0.01$). The control groups, MSNs and 1X PBS, released amines comparable to baseline noise for 2 and 4% gelatin (Fig. 4D and E). For 8% gelatin, MSN and DBPC HMSN treated hydrogels released significantly more amines at 3.6% duty cycle compared to 0% ($*p < 0.05$), whereas 1X PBS treated gels showed no significant change (Fig. 4F). The high baseline for 1X PBS at 0% duty cycle could be attributed to gel degradation during handling.

The considerable amine release in all 8% gelatin samples suggests that the dense polymer network amplifies whatever mechanical disruption occurs, whether from weak cavitation, acoustic streaming, or direct mechanical stress. Studies of sonication-induced bond scission in macromolecular systems have shown that ultrafast shear flow created by cavitation cleaves polymer chains, with the scission rate and resulting fragment size dependent on polymer architecture.[42] Furthermore, high-power probe ultrasonication (200–400 W) has been shown broadly to promote peptide-bond scission in gelatin, leading to increased free-amine release, in agreement with TNBS assay results.[43] Similarly, 750 W ultrasound treatment at 60% amplitude (20 kHz) of edible bird's nest (a glycoprotein similar to gelatin) significantly increased α-amino group content, indicating peptide

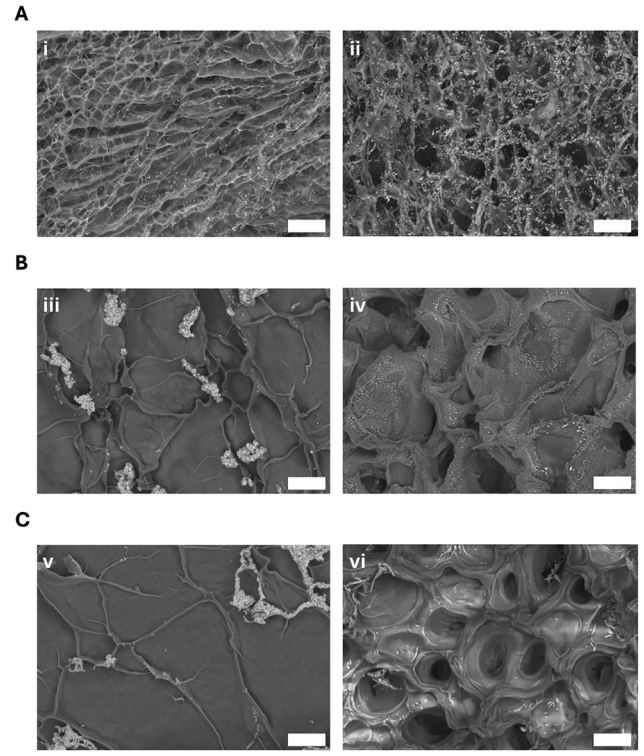

Fig. 5 Scanning electron microscopy images of untreated (left panel: i, iii, & v) and treated (right panel: ii, iv, & vi) (A) 2% gelatin (2.5% duty cycle), (B) 4% gelatin (2.5% duty cycle), and (C) 8% gelatin treated (3.6% duty cycle) with DBPC HMSNs. Scale bar = 20 μm.

bond cleavage.[44] It can be surmised that application of mechanical force in the stiffer gels affects the individual chains more because the denser structure transfers the mechanical actuation to the chains rather than dampening them through chain movement.

3.8. Structural changes observed by SEM

Microscopic analysis was then performed to visualize the resulting structural changes in the hydrogel network. SEM analysis of 1 mm-thick slices taken from the bottom of each gel post-treatment revealed striking gelatin concentration-dependent morphological changes (Fig. 5 and Fig. S9, S10). In 2% gelatin, all treatments (DBPC HMSNs, MSNs, and 1X PBS) added new micron scale pores to the porous, layered native structure. This structural disruption correlated with a significant increase in volume-weighted diameter for gels treated with HIFU and DBPC HMSNs (from 2 to 3.3 μm, $^{**}p < 0.01$, Fig. S11A), suggesting the formation of larger pore structures. These visible defects align with the significant amine release observed in TNBS assays, though the sparse distribution of damage explains why bulk modulus remained unchanged.

In 4% gelatin, all treatments produced microporous structures, with HIFU treatment with DBPC HMSNs producing the most uniform pore distribution (Fig. 5B). However, only DBPC HMSN showed an increase in volume-weighted diameter under 2.5% duty cycle (from 2.8 to 3.5 μm, $^{*}p < 0.05$, Fig. S11B), while MSN and 1X PBS remained unchanged. This intermediate gel concentration showed molecular damage (amine release) without mechanical weakening, indicating the network retained sufficient connectivity despite local disruption.

For 8% gelatin, while untreated samples showed smooth surfaces, HIFU treatment induced microscale structures across all groups, with gels treated with DBPC HMSNs and HIFU producing the most uniform circular pores (Fig. 5C). The volume-weighted diameter measurements showed no significant changes (Fig. S11C), though MSN and 1X PBS treatments trended toward smaller values. The organized honeycomb morphology in DBPC HMSN 8% gelatin, occurring alongside modulus reduction and amine release, indicates that stiff polymer networks fail differently than softer ones under HIFU stress. Whether this regular patterning represents an intrinsic mechanical response or an artifact requires further investigation. Additionally, higher-resolution techniques are needed to determine whether the damage from HIFU produces distributed nanoscale cavities or other forms of sub-resolution defects.

4. Conclusions

This study used gelatin hydrogels as a tunable model system because their viscoelasticity can be matched to the relevant range of many biological tissues.[45,46] Within this model system, it was demonstrated that DBPC HMSNs harness inertial cavitation to enable ultrasound-triggered nanoparticle motion through viscoelastic gelatin hydrogels. As hydrogel concentration increased from 2% to 8%, the required duty cycle for penetration rose from 0.5% to 3.6%. Simultaneously, penetration areas decreased due to increased mechanical resistance and ultrasound attenuation in denser networks. Multi-scale characterization revealed distinct failure modes. Soft hydrogels (2–4% gelatin) developed large cavities with significant amine release indicating molecular damage yet maintained bulk mechanical properties. In contrast, stiff 8% gelatin exhibited organized honeycomb structures, up to ~40% modulus reduction, and amine release across all treatment groups, including non-cavitating controls. These concentration-dependent responses suggest that matrix stiffness fundamentally alters how hydrogels respond to acoustic stress.

These findings have important implications for therapeutic translation. Cavitation-enhanced delivery remains effective across tested hydrogel stiffnesses, but the resulting damage patterns differ. In soft hydrogels, cavitation produces discrete microchannels that leave the surrounding matrix intact; in stiffer gels, however, those channels enlarge and interconnect into broad cavities, reflecting bulk material weakening. Future work should investigate whether biological tissues exhibit similar stiffness-dependent damage patterns, as bulk weakening may present a safety concern for treatment of dense tissues. To mitigate this weakening, one could employ strategies such as real-time acoustic monitoring to control cavitation,[47,48] optimizing pulse sequences to minimize energy delivery,[49,50] and incorporating longer rest periods between pulses to allow for thermal dissipation.

Finally, it should be noted that gelatin as a model tissue does not reproduce the complex architectural and acoustic

heterogeneity of *in vivo* barriers. Consequently, the acoustic variations in real biological tissues will likely alter ultrasound propagation and transport outcomes compared to this idealized model. One question in particular is the stability of resulting transport pathways formed by propelled particles. Here, sample drying upon hydrogel sectioning prevented a direct time-course analysis of pathway stability. However, for a clinically relevant benchmark, analogous microchannels created in skin by microneedles are reported to have functional half-lives of 20–66 hours, a lifetime governed by active biological repair mechanisms.[51,52]

Author contributions

The manuscript was written through contributions of all authors. All authors have given approval to the final version of the manuscript.

Conflicts of interest

There are no conflicts to declare.

Data availability

Raw images are available on request.

Supplementary information: materials and methods, HIFU interaction with negative controls, temperature measurements, penetration area, additional modulus data, SEM images and analysis. See DOI: **https://doi.org/10.1039/d5tb01702e**.

Acknowledgements

This work was supported by NSF 2025547. T. B. A. was supported by a Graduate Assistance in Areas of National Need (GAANN) fellowship (P200A210111). The imaging work was performed at the BioFrontiers Institute's Advanced Light Microscopy Core (RRID: SCR_018302). Laser scanning confocal microscopy was performed on a Nikon A1R microscope supported by NIST-CU Cooperative Agreement award number 70NANB15H226. The authors thank Dr Joe Dragavon for training on confocal microscopy, and Dr Jian Wei Tay of the BioFrontiers Advanced Light Microscopy Core for helpful discussions regarding the hydrogel transport setup and quantification. The authors also thank Lillian Mortensen for advice on SEM imaging of hydrogels. For exploratory studies, gels and membranes were imaged with the Typhoon 5 imager in the Shared Instruments Pool (RRID: SCR_018986) of the Department of Biochemistry at the University of Colorado Boulder. The authors also thank Dr Annette Erbse for training on the Typhoon imager. The Typhoon 5 was funded by NIH Shared Instrumentation Grant S10OD034218-01. The authors thank the Characterization Facility within Colorado Shared Instrumentation in Nanofabrication and Characterization (COSINC-CHR) for use of their Hitachi TM-4000Plus II tabletop SEM, and Dr Adrian Gestos for training. The authors thank Prof. Christopher Bowman for use of his Ares G-2 rheometer and Prof. Todd W. Murray for use of his Sonic Concepts H-101 HIFU transducer. The authors also thank Dr Meagan Arguien for training on the Bowman lab rheometer, and Dr Alex Kang and Dr Nikolas Di Caprio for helpful discussions on measuring local changes to material modulus. Illustrations were created with BioRender.com. ChatGPT and Claude were used to generate and edit code for data analysis and plotting, which are included in a relevant Github repository.[32]

Notes and references

1 K. Retz, S. Kotopoulis, T. Kiserud, K. Matre, G. E. Eide and R. Sande, *Ultrasound Obstetrics Gynecol.*, 2017, **50**, 236–241.
2 W. J. Tyler, Y. Tufail, M. Finsterwald, M. L. Tauchmann, E. J. Olson and C. Majestic, *PLoS One*, 2008, **3**, e3511.
3 S. Mitragotri, D. Blankschtein and R. Langer, *Pharm. Res.*, 1996, **13**, 411–420.
4 P. Tharkar, R. Varanasi, W. S. F. Wong, C. T. Jin and W. Chrzanowski, *Front. Bioeng. Biotechnol.*, 2019, **7**, DOI: **10.3389/fbioe.2019.00324**.
5 A. Copelan, J. Hartman, M. Chehab and A. M. Venkatesan, *Semin. Interv. Radiol.*, 2015, **32**, 398–415.
6 J. Chen, Y. Li, Z. Wang, P. McCulloch, L. Hu, W. Chen, G. Liu, J. Li and J. Lang, Committee of the Clinical Trial of HIFU versus Surgical Treatment for Fibroids, *BJOG*, 2018, **125**, 354–364.
7 L. Poissonnier, J.-Y. Chapelon, O. Rouvière, L. Curiel, R. Bouvier, X. Martin, J. M. Dubernard and A. Gelet, *Eur. Urol.*, 2007, **51**, 381–387.
8 H. Baek, D. Lockwood, E. J. Mason, E. Obusez, M. Poturalski, R. Rammo, S. J. Nagel and S. E. Jones, *Front. Neurol.*, 2022, **13**, 880814.
9 M. J. Stone, V. Frenkel, S. Dromi, P. Thomas, R. P. Lewis, K. C. Li, M. Horne and B. J. Wood, *Thromb. Res.*, 2007, **121**, 193–202.
10 Z. Xu, T. L. Hall, E. Vlaisavljevich and F. T. Lee, *Int. J. Hyperthermia*, 2021, **38**, 561–575.
11 J. Yang, H. C. Cramer, S. Buyukozturk and C. Franck, in *Dynamic Behavior of Materials*, ed.S. Mates and V. Eliasson, Springer International Publishing, Cham, 2022, Vol. 1, pp. 47–52.
12 K. A. Mahmud, F. Hasan, M. I. Khan and A. Adnan, *Sci. Rep.*, 2020, **10**, 9635.
13 D. L. Miller, N. B. Smith, M. R. Bailey, G. J. Czarnota, K. Hynynen and I. R. S. Makin, Bioeffects Committee of the American Institute of Ultrasound in Medicine, *J. Ultrasound Med.*, 2012, **31**, 623–634.
14 C. C. Coussios, C. H. Farny, G. Ter Haar and R. A. Roy, *Int. J. Hyperthermia*, 2007, **23**, 105–120.
15 A. Yildirim, D. Shi, S. Roy, N. T. Blum, R. Chattaraj, J. N. Cha and A. P. Goodwin, *ACS Appl. Mater. Interfaces*, 2018, **10**, 36786–36795.
16 A. Yildirim, R. Chattaraj, N. T. Blum, D. Shi, K. Kumar and A. P. Goodwin, *Adv. Healthcare Mater.*, 2017, **6**, 1700514.
17 R. Chapla, K. T. Huynh and C. E. Schutt, *Pharmaceutics*, 2022, **14**, 2396.

18 S. Lu, P. Zhao, Y. Deng and Y. Liu, *Pharmaceutics*, 2022, **14**, 480.
19 H. Ashar and A. Ranjan, *Pharmacol. Ther.*, 2023, **244**, 108393.
20 G. Shakya, M. Cattaneo, G. Guerriero, A. Prasanna, S. Fiorini and O. Supponen, *Adv. Drug Delivery Rev.*, 2024, **206**, 115178.
21 M. K. Badawe, K. Nasr, L. Jiang, X. Lu, S. Cheng and W. Qiu, *Front. Bioeng. Biotechnol.*, 2024, **12**, 1276143.
22 F. S. Rawnaque and J. C. Simon, *J. Acoust. Soc. Am.*, 2022, **152**, 3502–3513.
23 A. Bampouli, Q. Goris, J. Van Olmen, S. Solmaz, M. Noorul Hussain, G. D. Stefanidis and T. Van Gerven, *Ultrason. Sonochem.*, 2023, **97**, 106444.
24 E. L. Madsen, M. A. Hobson, H. Shi, T. Varghese and G. R. Frank, *Phys. Med. Biol.*, 2005, **50**, 5597–5618.
25 M. Czerner, L. S. Fellay, M. P. Suárez, P. M. Frontini and L. A. Fasce, *Procedia Mater. Sci.*, 2015, **8**, 287–296.
26 H. Mehdi-Sefiani, E. Chicardi, A. Romero and V. M. Perez-Puyana, *Polymers*, 2024, **16**, 1842.
27 J. Liu, B. Zhang, L. Li, J. Yin and J. Fu, *Bioact. Mater.*, 2021, **6**, 219–229.
28 L. E. Jansen, N. P. Birch, J. D. Schiffman, A. J. Crosby and S. R. Peyton, *J. Mech. Behav. Biomed. Mater.*, 2015, **50**, 299–307.
29 W.-C. Yeh, P.-C. Li, Y.-M. Jeng, H.-C. Hsu, P.-L. Kuo, M.-L. Li, P.-M. Yang and P. H. Lee, *Ultrasound in Med. Biol.*, 2002, **28**, 467–474.
30 S. Budday, R. Nay, R. de Rooij, P. Steinmann, T. Wyrobek, T. C. Ovaert and E. Kuhl, *J. Mech. Behav. Biomed. Mater.*, 2015, **46**, 318–330.
31 F. Liu, J. D. Mih, B. S. Shea, A. T. Kho, A. S. Sharif, A. M. Tager and D. J. Tschumperlin, *J. Cell Biol.*, 2010, **190**, 693–706.
32 T. B. Alina, Available online: **https://github.com/ThundaNann/hydrogel_transport**.
33 T. B. Alina, S. A. Saemundsson, L. E. Mortensen, Y. Xu, J. W. Medlin, J. N. Cha and A. P. Goodwin, *Adv. Funct. Mater.*, 2024, 2412344.
34 R. Ellerbrock, M. Stein and J. Schaller, *Sci. Rep.*, 2022, **12**, 11708.
35 T. R. Ausec, L. L. Carr, T. B. Alina, N. B. Day, A. P. Goodwin and C. W. I. Shields, *ACS Appl. Nano Mater.*, 2024, **7**, 19109–19117.
36 T. B. Alina, H. B. Kirkpatrick, N. M. Bower, S. D. Curry, T. R. Ausec, S. A. Saemundsson, E. N. Mueller, C. W. I. Shields, J. N. Cha and A. P. Goodwin, *ACS Appl. Nano Mater.*, 2023, **6**, 13720–13729.
37 A. Clark, S. Bonilla, D. Suo, Y. Shapira and M. Averkiou, *Ultrasound Med. Biol.*, 2021, **47**, 2296–2309.
38 P. J. Moncure, Z. C. Simon, J. E. Millstone and J. E. Laaser, *J. Phys. Chem. B*, 2022, **126**, 4132–4142.
39 B. Amsden, *Macromolecules*, 1998, **31**, 8382–8395.
40 W. Kang and M. Raphael, *Sci. Rep.*, 2018, **8**, 15840.
41 J. Yang, A. Tzoumaka, K. Murakami, E. Johnsen, D. L. Henann and C. Franck, *Phys. Rev. E*, 2021, **104**, DOI: **10.1103/PhysRevE.104.045108**.
42 Y. Li, Z. Niu, J. Burdyńska, A. Nese, Y. Zhou, Z. S. Kean, A. V. Dobrynin, K. Matyjaszewski, S. L. Craig and S. S. Sheiko, *Polymer*, 2016, **84**, 178–184.
43 L. He, Y. Gao, X. Wang, L. Han, Q. Yu, H. Shi and R. Song, *Ultrason. Sonochem.*, 2021, **78**, 105738.
44 K. Chantakun and S. Benjakul, *J. Food Sci. Technol.*, 2022, **59**, 3908–3917.
45 P. Chen, A. M. A. O. Pollet, A. Panfilova, M. Zhou, S. Turco, J. M. J. den Toonder and M. Mischi, *Ultrasound Med. Biol.*, 2022, **48**, 124–142.
46 A. Jawli, W. Aldehani, G. Nabi and Z. Huang, *Bioengineering*, 2024, **11**, 620.
47 N. McDannold, P. Y. Wen, D. A. Reardon, S.-M. Fletcher and A. J. Golby, *J. Control Release*, 2024, **372**, 194–208.
48 C.-Y. Chien, Y. Yang, Y. Gong, Y. Yue and H. Chen, *BME Front*, 2022, 9867230.
49 Q. Zhang, Y. Zhu, G. Zhang, H. Xue, B. Ding, J. Tu, D. Zhang and X. Guo, *Ultrason. Sonochem.*, 2024, **110**, 107051.
50 S. Bae, K. Liu, A. N. Pouliopoulos, R. Ji, S. Jiménez-Gambín, O. Yousefian, A. R. Kline-Schoder, A. J. Batts, F. N. Tsitsos, D. Kokossis, A. Mintz, L. S. Honig and E. E. Konofagou, *Theranostics*, 2024, **14**, 4519–4535.
51 J. Gupta, H. S. Gill, S. N. Andrews and M. R. Prausnitz, *J. Control Release*, 2011, **154**, 148–155.
52 A. T. Ogunjimi, J. Carr, C. Lawson, N. Ferguson and N. K. Brogden, *Sci. Rep.*, 2020, **10**, 18963.